Applied Radiation and Isotopes 226 (2025) 112233

Contents lists available at ScienceDirect

Applied Radiation and Isotopes

journal homepage: www.elsevier.com/locate/apradiso

A dosimetric and biological model for neutron capture therapy (NCT) experiments

A. Kalamara [a,*], I.E. Stamatelatos [a], K.L. Stefanopoulos [a], J.A. Kalef-Ezra [b], A.G. Georgakilas [c], R.D. Stewart [d], V. Rangos [c,e], K.D. Knudsen [f], G. Helgesen [f], P. Trtik [g], D. Mannes [g], J. Hovind [g], A. Kaestner [g], M. Strobl [g], M. Vinš [h], V. Klupák [h], M. Rabochová [h], J. Šoltés [h], J. Milčák [h], M. Grigalavicius [i,j], T.A. Theodossiou [i]

[a] National Centre for Scientific Research "Demokritos", 15310, Aghia Paraskevi, Greece
[b] Medical Physics Laboratory, School of Health Sciences, University of Ioannina, Ioannina, 45110, Greece
[c] Department of Physics, School of Applied Mathematical and Physical Sciences, National Technical University of Athens (NTUA), Zografou Campus, 15780, Athens, Greece
[d] Department of Radiation Oncology, School of Medicine, University of Washington, Seattle, WA, 98195-604, USA
[e] Medical Physics Laboratory, School of Medicine, University of Athens, Greece
[f] Institute for Energy Technology (IFE), Instituttveien 18, 2027, Kjeller, Norway
[g] Laboratory for Neutron Scattering and Imaging (LNS), Paul Scherrer Institut (PSI), Forschungsstrasse 111, 5232, Villigen, Switzerland
[h] Research Centre Řež, Hlavní 130, 250 68, Husinec-Řež, Czech Republic
[i] Department of Radiation Biology, Institute for Cancer Research, Oslo University Hospital, 0379 Oslo, Norway
[j] Laser Research Center, Faculty of Physics, Vilnius University, Saulėtekio av. 9, III bld., LT 10222 Vilnius, Lithuania

ARTICLE INFO

Keywords:
Neutron capture therapy
High LET
MCNP
MCDS
Microdosimetry
RBE

ABSTRACT

A hybrid Monte Carlo approach using MCNP in combination with the cell-level code Monte Carlo Damage Simulation (MCDS) is presented to support the design and analysis of experiments for the evaluation of gadolinium (Gd) based agents in neutron capture therapy (NCT). Monoenergetic neutrons (0.025 eV–15 MeV) and polyenergetic neutron beams from NEUTRA, ICON (PSI, Switzerland), and HK1 (LVR-15, Czech Republic) were used to estimate the relative biological effectiveness (RBE) of NCT for the biologically critical endpoint of DNA double strand break (DSB) production relative to ^{60}Co γ-rays. Moreover, microdosimetric spectra of protons, electrons, alpha particles and heavy recoils were determined for the aforementioned neutron beams, to enhance the interpretation of energy deposition in subcellular structrures. The proposed, hybrid model and methodology builds on well-validated dosimetry and biophysical models at different spatial scales to create a versatile and generalized framework to estimate dosimetric parameters and RBE. This approach facilitates comparisons between NCT and low linear energy transfer (LET) radiation alternatives.

1. Introduction

Neutron capture therapy (NCT) uses high Linear Energy Transfer (LET) radiation from secondary particles to target tumors at a cellular level. NCT involves a two-step process: first, the patient is injected with a drug containing a stable isotope with a high neutron capture cross section, that selectively accumulates to the tumor. Next, the tumor is irradiated with neutrons, which penetrate in tissue and are captured by the stable isotope, generating high LET secondary ions with a large potential to damage tumor cells. Currently, clinical applications of NCT are limited to Boron Neutron Capture Therapy (BNCT). In BNCT, a thermal neutron capture reaction with ^{10}B (3,837 b cross section) is used to produce recoil ^{4}He and ^{7}Li nuclei (Dymova et al., 2020). As an alternative to ^{10}B, ^{157}Gd (15.65 % abundance in natural Gd) has been proposed as a promising candidate for NCT because of its very high thermal neutron capture cross section of 254,164 b (Shih and Brugger, 1992; Ho et al., 2020; Deagostino et al., 2016; Enger et al., 2013; Cerullo et al., 2009; De Stasio et al., 2005; Goorley et al., 2004; Miller et al.,

This article is part of a special issue entitled: ANP 2024 published in Applied Radiation and Isotopes.

* Corresponding author.
E-mail address: a.kalamara@ipta.demokritos.gr (A. Kalamara).

https://doi.org/10.1016/j.apradiso.2025.112233
Received 7 February 2025; Received in revised form 1 September 2025; Accepted 3 October 2025
Available online 4 October 2025

1993; Brugger and Shih, 1989; Allen et al., 1989). Moreover, Gd compounds, such as Gd-diethylenetriaminepentaacetic acid (Gd-DTPA) have been widely used clinically as contrast agents for Magnetic Resonance Imaging and have shown high uptake by tumor cells in the brain (Yasui et al., 2008; Ho et al., 2022).

In Fig. 1, a summary of the ^{157}Gd neutron capture reaction (Q = 7.94 MeV) and its decay routes are presented. More specifically, 99 % of the energy released is emitted as prompt-γ radiation, with average energy 2.4 MeV and with the most intense γ-rays being at 79.5 and 181.9 keV. The remainder 1 % of the energy is released through internal conversion (IC) and consequently as characteristic X-ray or Auger/Coster-Kronig electrons emission. The IC electrons are produced with a 0.69 total yield and 66.5 keV average energy. In addition, five Auger electrons with 0.85 keV average energy and 0.84 X-rays with 12.77 keV average energy are produced per capture during ^{158}Gd* de-excitation (Ali et al., 1994; Van Delinder et al., 2020; Sakurai et al., 2002). More details on IC and Auger electron energies from ^{157}Gd capture are given in refs. (Harms et al., 1974; Coghlan et al., 1973; Schultz et al., 2010). Although most of the excitation energy of ^{158}Gd is mainly released as gamma radiation, IC and Auger electrons are anticipated to have an important role in Gadolinium NCT, since the released electrons have a high LET (300 keV/μm) and a short range in tissue (0–150 nm) and therefore, can effectively deposit their energy at cellular and sub-cellular level (Golshani et al., 2022).

This study presents a detailed macro- and micro-scale dosimetry and biophysical model for the NCT irradiation of cell cultures. The model was developed to support a series of experiments evaluating novel gadolinium (Gd) agents proposed for neutron capture therapy (NCT). The primary objective of the current study is to investigate *a priori* whether the introduction of Gd might enhance the cell-killing effectiveness of neutron beams under specific irradiation conditions.

Due to the lack of electronic equilibrium for the proposed experimental design, measuring or calculating the absorbed dose within the target cell volume is very challenging. An accurate evaluation of dose requires Monte Carlo simulations for specific, macro-scale experimental designs. The presented model evaluates dose and relative biological effectiveness (RBE) in a monolayer cell culture geometry, along with the surrounding medium. The dose delivered to cell cultures is calculated at the level of a 2 μm-diameter sphere, representing the cell nucleus.

The simulations aim to generate microdosimetric spectra for secondary electrons, protons and heavy (Z > 1) particles produced by monoenergetic neutron beams spanning an energy range from 0.025 eV to 15 MeV. The study also simulated the polyenergetic neutrons relevant to a specific NCT experimental setup. This approach enables the analysis of secondary particle energy deposition at the microscopic level for a wide variety of irradiation geometries and neutron sources. Additionally, the RBE for DNA double strand breaks induction is evaluated for a proposed experiment and facility-specific design.

2. Simulations

2.1. Neutron beams

Simulations were carried out using the MCNP 6.1 code (MCNP6 Release Overview). Monoenergetic neutron beams were modelled at the energy range from 0.025 eV to 15 MeV. Moreover, the neutron spectra of interest comprise the NEUtron Transmission Radiography (NEUTRA) (Lehmann et al., 2001) and the Imaging with Cold Neutrons (ICON) (Kaestner et al., 2011) instruments at the Swiss Spallation Neutron Source (SINQ) of the Paul Scherrer Institut (PSI), as well as the HK1 beam line at the LVR-15 reactor at Research Centre Řež (Marek et al., 2014). The respective neutron energy spectra considered for the simulations are shown in Fig. 2.

2.2. Irradiation geometry

The simulated irradiation geometry for a single well of 6 × 3 well-plate holder (ibidi^{TM}) for the proposed cell culture experiments is shown in Fig. 3. The well-plate is composed of polyethylene with a thin entrance window of 180 μm thickness. In the well, a cell monolayer 20 μm thick with a 4.3 mm water layer is modelled. The cell monolayer volume is filled either with soft tissue equivalent material (ICRP composition, see Table 1) with density 1 g/cm^3, (ICRP) or with soft tissue loaded with ^{nat}Gd. The cell monolayer is modelled as an

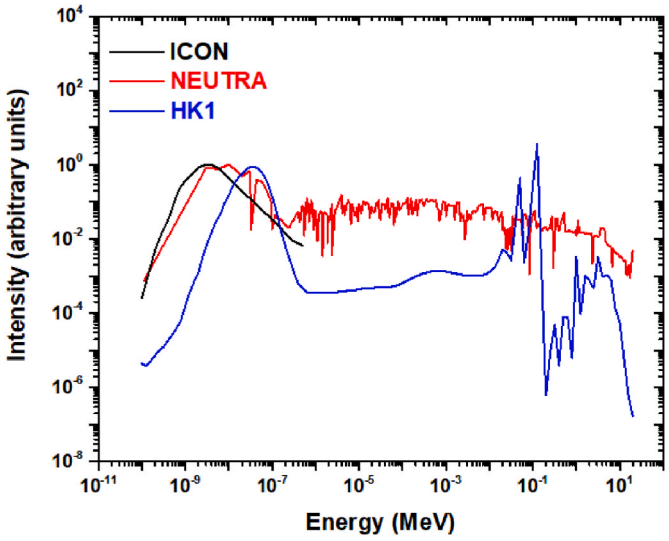

Fig. 2. *Neutron spectra (in arbitrary units) of ICON (black line), NEUTRA (red line) instruments* and HK-1 beam line (red line) used in the MCNP simulations. (For interpretation of the references to colour in this figure legend, the reader is referred to the Web version of this article.)

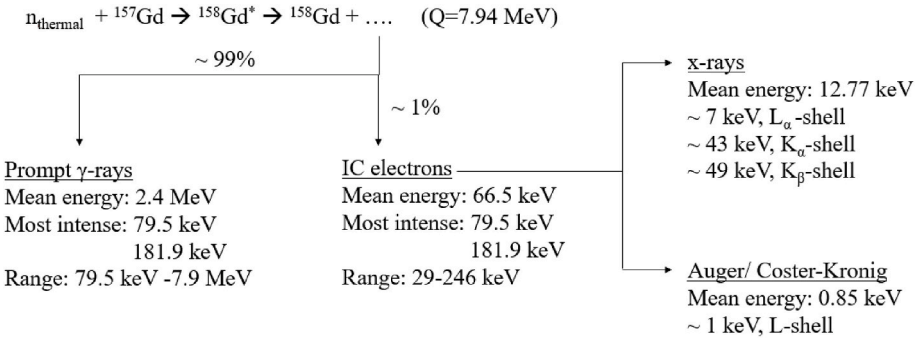

Fig. 1. ^{157}Gd neutron capture products.

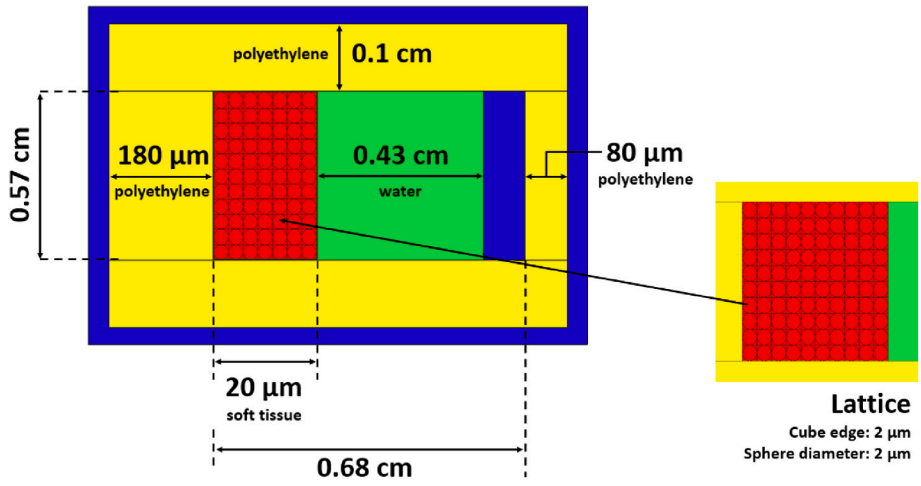

Fig. 3. MCNP simulated cell culture geometry (not to scale). The scoring volume (shown in red) is the 20 µm cell monolayer, which is modelled as a lattice consisting of an array of 2 µm in diameter successive spheres representing individual cell targets. (For interpretation of the references to colour in this figure legend, the reader is referred to the Web version of this article.)

Table 1
ICRP soft-tissue composition, with density 1 g/cm^3.

Element	Atomic number	Fraction by weight
H	1	0.104472
C	6	0.232190
N	7	0.024880
O	8	0.630238
Na	11	0.001130
Mg	12	0.000130
P	15	0.001330
S	16	0.001990
Cl	17	0.001340
K	19	0.001990
Ca	20	0.000230
Fe	26	0.000050
Zn	30	0.000030

orthogonal lattice containing 2 µm in diameter successive spheres, representing the cell target. The spherical volumes used as scoring tallies to perform the microdosimetry calculations are described in the next section. Neutron scattering from adjacent materials and photons originating directly from the reactor core or photons produced by neutron interactions with shielding and beam modifying materials and the irradiation room are not taken into account.

2.3. Libraries and energy cut-offs

The default cross section library of the MCNP 6.1, ENDF-VII.1 was used for all simulations, however the EPRDATA12 (Electron-Photon-Relaxation DATA) was invoked by using the ".12p" cross section identifier on material cards, in order to enable photoatomic cross sections that allow for the transmission of photons and electrons at energies below 1 keV. A cut-off energy of 0 eV was used for neutrons. A cut-off energy of 50 eV was used for photons and electrons. The lowest possible cut-off energy allowed in MCNP of 1 keV was used for protons and heavier (Z > 1) ions. Moreover, the thermal neutron treatment was implemented for hydrogen in H_2O ("lwtr.60t") and in polyethylene ("poly.60t"), respectively.

3. Microdosimetry calculations

The stochastic distribution of the energy deposition of all primary and secondary particles at cellular and subcellular level was assessed. The basic microdosimetric quantities: specific energy, $z(Gy)$, and lineal energy, $y(keV/\mu m)$, i.e. the stochastic analogs of dose and linear energy transfer (LET), respectively (Santa Cruz, 2016; Tung, 2015) are given by the following expressions:

$$z(Gy) = \frac{\varepsilon\ (J)}{m\ (kg)} = \frac{energy\ imparted\ by\ one\ or\ more\ events\ in\ a\ site\ of\ mass}{mass} \quad (1)$$

$$y(keV/\mu m) = \frac{\varepsilon\ (keV)}{\bar{l}\ (\mu m)} = \frac{energy\ imparted\ in\ one\ event}{mean\ chord\ length} \quad (2)$$

where the mean chord length ($\bar{l}$) in a sphere of diameter d is given by:

$$\bar{l} = 2 * d/3 \quad (3)$$

The frequency distribution of the lineal energy, $f(y)$, that corresponds to the probability that a measurement will have a lineal energy between y and $y + dy$ is given by:

$$f(y_i) = \frac{n_i}{\sum_i n_i} \quad (4)$$

where n_i is the number of events depositing the same energy per µm. The non-stochastic quantity called "frequency-mean lineal energy, $\bar{y}_F$", is given by:

$$\bar{y}_F(keV/\mu m) = \int_0^\infty y\, f(y)\, dy = \frac{\sum_i y_i\, n_i}{\sum n_i} = \frac{1000}{\bar{l}(\mu m)}\ \frac{\sum_i \varepsilon_i(MeV)\, n_i}{\sum n_i} \quad (5)$$

The y value that contributes the most to the energy released in the sampling volume is the "dose-mean lineal energy, $\bar{y}_D$":

$$\bar{y}_D(keV/\mu m) = \int_0^\infty y\, d(y)\, dy \xrightarrow{d(y)=\frac{y\, f(y)}{\bar{y}_F}} \bar{y}_D = \int_0^\infty \frac{y^2}{\bar{y}_F} f(y)\, dy = \frac{1000}{\bar{l}(\mu m)} \frac{\sum_i [\varepsilon_i(MeV)]^2\, n_i}{\sum \varepsilon_i(MeV)\, n_i} \tag{6}$$

where $d(y)$ is the lineal energy distribution of absorbed dose. The most common way to graphically represent the absorbed dose, $d(y)$, is to plot $y\, d(y)$ in a logarithmic scale. To estimate it using MCNP, three scoring (tally) cards were used, namely those for: i) the neutron flux (f4:n), ii) the energy deposition (f6 for protons, heavy ions and electrons) and iii) the pulse height (f8) coupled with f6, along with an anticoincidence pulse height card (ft8 phl) for counting single-event of imparted energy in the targets, 2 μm in diameter. Additionally, an e8 card was used (e8 0.0 0.00001 0.0006 250log 60), so that 250 logarithmic lineal energy bins are defined, including 50 bins per decade from 0.45 to 45000 keV/μm. In order to plot the microdosimetric spectra, $y\, d(y)$ is calculated by the following formula:

$$y_i\, d(y_i) = \frac{\varepsilon_i\, n_i}{\sum_i \varepsilon_i\, n_i} \left(\frac{1}{log(\varepsilon_i/\varepsilon_{i-1})} \right) \tag{7}$$

where n_i was substituted by the output of the f8 tally combined with the anticoincidence pulse height card and the sum was performed for i up to 250 and for each particle type taken into account in the simulations (electrons, protons, alpha particles, heavy ions).

The single collision KERMA factor to the specific target can be determined by:

$$\frac{K}{\Phi} = \frac{1.6 \times 10^{-13} \left(\frac{Joule}{MeV}\right)}{\frac{1}{1000}\left(\frac{kg}{g}\right)} \left(\frac{\bar{l}(\mu m)}{\Phi \left(\frac{n}{cm^2\, n'}\right) \rho \left(\frac{g}{cm^3}\right) V(cm^3)} \right) \sum_i \frac{\varepsilon_i(MeV)}{\bar{l}(\mu m)} n_i\, 10^2 \Rightarrow \frac{K}{\Phi}(cGy\, cm^2) = \frac{1.6 \times 10^{-8}}{\Phi\ \rho\ V} \sum_i \varepsilon_i\, n_i \tag{8}$$

where Φ is the beam flux impinging on the sampling volume (in neutrons/cm^2 per source particle), ρ the material density (in g/cm^3), V the volume (in cm^3) and 10^2 the conversion factor from Gy to cGy.

The absorbed dose is determined by:

$$\frac{D}{\Phi} = \frac{E_{deposited}\left(\frac{MeV}{g\ n'}\right)}{\Phi \left(\frac{n}{cm^2\ n'}\right)} \frac{1.6 \times 10^{-13} \left(\frac{Joule}{MeV}\right)}{\frac{1}{1000}\left(\frac{kg}{g}\right)} \Rightarrow \frac{D}{\Phi} = \frac{E_{deposited}}{\Phi}\, 1.6 \times 10^{-10} \tag{9}$$

where $E_{deposited}$ is the energy deposition in MeV/g per source neutron calculated via the +f6 tally in the MCNP code, which takes into account all the particles of the simulation (Antoni et al., 2019).

The aforementioned method was applied to monoenergetic neutron beams as well as to the three beamlines of interest for the present study. As examples, the $y\, d(y)$ versus y graphs are given in Fig. 4(a) for monoenergetic 25 meV, 10 keV, 100 keV, 1 MeV and 10 MeV neutron beams. The observed spectral peaks include electrons, protons, alpha particles and heavy ions. The primary contributors to the microdosimetric spectra, across all neutron beam energies, except for 25 meV neutrons, are recoil protons from elastic scattering in hydrogen, ^{1}H(n,n')^{1}H. Other reactions for proton production are ^{16}O(n,p)^{16}N, ^{14}N(n,p)^{14}C, ^{14}N(n,n'p)^{13}C and ^{16}O(n,n'p)^{15}N. In the case of 25 meV neutrons, the proton contribution is much lower than the electron one and therefore, it can not be distinguished in the $y\, d(y)$ versus y graphs in Fig. 4.

As shown in Fig. 4(a), the centroids of the proton $y\, d(y)$ peaks of 10 keV to 1 MeV neutron beams shift to higher y values with increasing energy. In the case of 10 MeV beam, the peak becomes wider with the centroid towards lower lineal energy values. This behavior is attributed to the fact that the range of some secondary particles at this higher energy do not deposit all of their energy in the monolayer. For example,

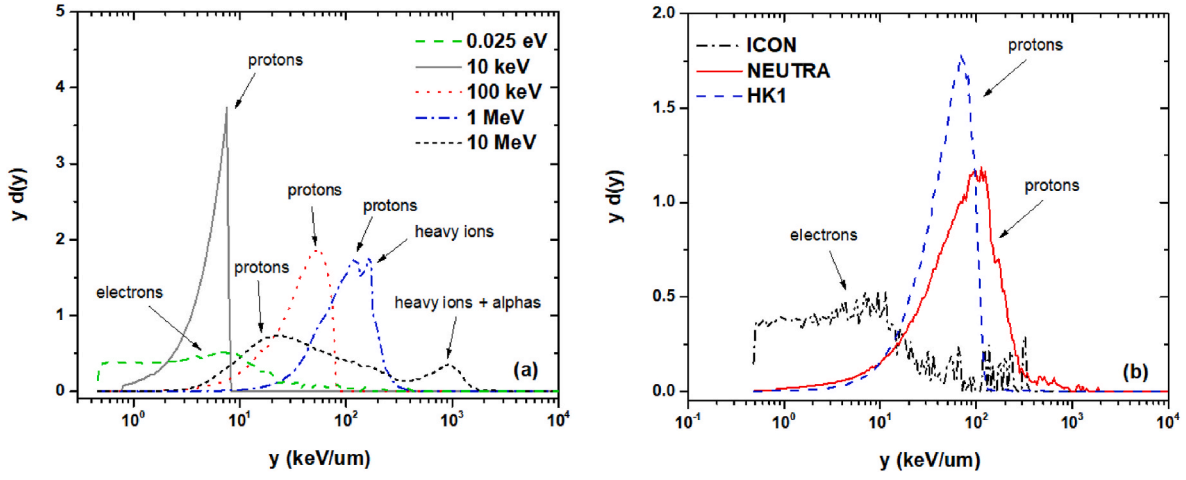

Fig. 4. Microdosimetric spectra for protons, electrons, alpha particles and heavy recoils, scored at the 2 μm diameter spheres inside the 20 μm thick cell monolayer containing soft tissue for some of (a) monoenergetic neutron beams, (b) ICON, NEUTRA and HK1 beams.

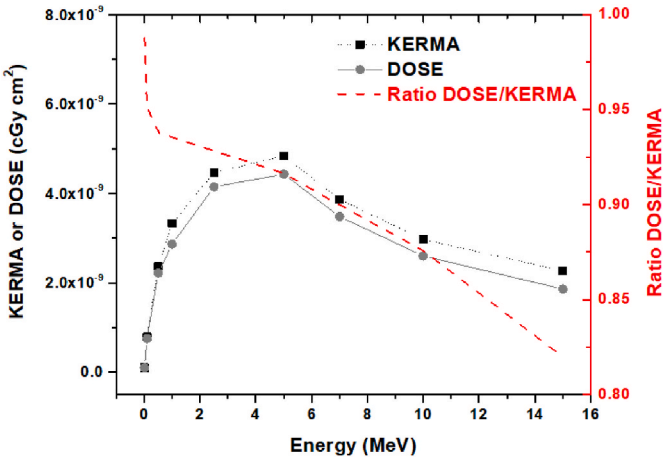

Fig. 5. KERMA factor (K/Φ), absorbed dose (D/Φ) with respect to neutron beam energy, for monoenergetic neutrons in monolayer cell cultures composed of soft tissue. The ratio of absorbed dose over KERMA (D/K) (y-axis) is shown to highlight the impact of charged particle equilibrium.

Table 2
KERMA (K/Φ), absorbed dose (D/Φ) and ratio of absorbed dose over KERMA (D/K) for cell monolayer containing soft tissue and for the HK1, NEUTRA and ICON facilities.

Neutron Spectrum	K/Φ (cGy cm^2)	D/Φ (cGy cm^2)	Ratio D/K
ICON	$(2.92 \pm 0.05) \times 10^{-12}$	$(2.13 \pm 0.07) \times 10^{-12}$	0.73 (3.6 %)
0.025 eV	$(1.93 \pm 0.01) \times 10^{-12}$	$(1.44 \pm 0.02) \times 10^{-10}$	0.75 (1.3 %)
NEUTRA	$(2.19 \pm 0.01) \times 10^{-10}$	$(2.03 \pm 0.01) \times 10^{-10}$	0.93 (0.6 %)
HK1	$(3.87 \pm 0.01) \times 10^{-10}$	$(3.67 \pm 0.01) \times 10^{-10}$	0.95 (0.4 %)

the range of 3 and 8 MeV protons is about 7 and 40 times larger than the thickness of the cell monolayer, respectively. Note that for energies above 1 MeV, heavy ions and alpha particles are also significant. The former include mainly N and O recoils, from ^{16}O(n,n'p)^{16}N and ^{16}O(n,n')^{16}O reactions as well as C nuclei produced by ^{14}N(n,p)^{14}C, ^{12}C(n,n')^{12}C, ^{16}O(n,α)^{13}C and ^{16}O(n,n'a)^{12}C reactions in soft tissue. The last two reactions are the ones responsible for the alpha particles production, for neutron energies above the reaction thresholds at 2.36 MeV and 7.61 MeV, respectively (QCalc).

In Fig. 4(b), microdosimetric spectra for the three neutron beams of interest are presented. In the case of cold neutrons (ICON), there is a wide peak centered at low y values (mainly 0.5–15 keV/μm), which is attributed to electrons that are produced either via knock-on reactions, Compton scattering, atomic deexcitations (internal conversion and Auger electrons), while the proton contribution from ^{14}N(n,p)^{14}C reaction is much lower and therefore can not be identified. For HK1 and NEUTRA neutron beams, protons are dominant with peak centroids at 70 and 110 keV/μm, respectively.

The single collision KERMA factor (K/Φ, Eq. (8)) and the absorbed dose (D/Φ, Eq. (9)) for simulations with the cell monolayer, are presented in Fig. 5 with respect to the neutron beam energy for monoenergetic neutrons. The corresponding values for the neutron beams of interest are summarized in Table 2.

As shown in Fig. 5, both KERMA and absorbed dose per unit neutron fluence in the simulated cellular nuclei increase with increasing neutron energy up to 5 MeV, while for higher energies, they gradually decrease, due to the small thickness of the cell monolayer. Moreover, the ratio of absorbed dose over KERMA is presented with a dotted red line, showing that there is a sharp decrease of the ratio for energies between 10 and 500 keV (from 0.99 to 0.94), while the decrease is more smooth at higher energies (from 0.94 at 0.5 MeV to 0.82 at 15 MeV). A value close to 1.00 means that all of the energy released in the soft tissue is absorbed in the scoring volume. However, this is not the case for higher energies. Thus, in case of 10 keV, the maximum value of the absorbed energy can be found by multiplying the y value corresponding to the right edge of the microdosimetric spectrum in Fig. 4(a), namely about 8 keV/μm, by the mean chord length 1.33 μm at the cell target.

Table 3
Comparison of the absorbed dose calculated for 0 and 1000 ppm concentration of ^{nat}Gd in soft tissue inside the cell monolayer and the corresponding ratio values.

Neutrons	D/Φ (cGy cm^2)		Ratio
	0 ppm ^{nat}Gd	1000 ppm ^{nat}Gd	Dose 1000 ppm/Dose 0 ppm
ICON	$(2.12 \pm 0.02) \times 10^{-12}$	$(2.33 \pm 0.02) \times 10^{-12}$	1.095 (1.4 %)
0.025 eV	$(1.44 \pm 0.02) \times 10^{-12}$	$(1.50 \pm 0.02) \times 10^{-12}$	1.039 (1.6 %)

4. Dosimetric effect of gadolinium

Simulations performed for the same geometry, but for a cell monolayer made of soft tissue equivalent material loaded with 1000 ppm of ^{nat}Gd, showed differences in absorbed dose only in the case of 0.025 eV neutrons and for the ICON neutron beams (Table 3). Consequently, for the tested cell monolayer geometry, the effect of Gd is present only for very low energy neutron beams. In order to achieve some effect at higher neutron energies, an appropriate moderating material could be used, such as heavy water.

5. Calculation of RBE

RBE is defined as the ratio of the absorbed dose of a reference radiation, usually low LET γ-rays or high-energy x-rays, to the dose of a higher LET test radiation, such as the radiation fields that arise in NCT. Due to the biological significance of processing of DNA double strand breaks (DSB) into chromosomal aberrations, DSB induction was used as a surrogate endpoint to assess the biological impact of Gd agents in NCT. In the present study, the RBE was defined (often denoted as RBE_{DSB}) as the ratio of the DSB yield (number of DSBs induced per 10^9 base pairs) for the radiation of interest in the specific geometry to the DSB yield for ^{60}Co γ-rays. The Monte Carlo Damage Simulation (MCDS) software replicates results from a wide range of experimental studies as well as the results of single-event Monte Carlo simulations (Semenenko and Stewart, 2004, 2006; Stewart et al., 2011). The MCDS was combined with larger-scale MCNP simulations (Stewart et al., 2015) to estimate the DSB yield for the low-LET reference radiation and for the higher LET radiation experiments that mimic NCT. The MCDS accounts for direct and indirect effects of radiation on the formation of clusters of damaged nucleotides in DNA by various types of ionizing radiation, including electrons, protons and heavier ions (Stewart et al., 2011). The MCDS has the ability to simulate cluster induction as a function of O_2 level, particle type ($Z < 26$ ions) and kinetic energies from a few eV for electrons and of about 1 keV for $Z > 1$ ions up to kinetic energies in the GeV energy

Table 4
The MCDS predicted ratio of SSB per DSB and total cluster yield for ^{60}Co γ-rays under aerobic and hypoxic conditions.

O_2 concentration	SSB (Gy^{-1} · Gbp^{-1})	DSB (Gy^{-1} · Gbp^{-1})	TOTAL (Gy^{-1} · Gbp^{-1})
20 % (aerobic)	187	8.19	619
0.1 % (hypoxic)	130	3.66	457

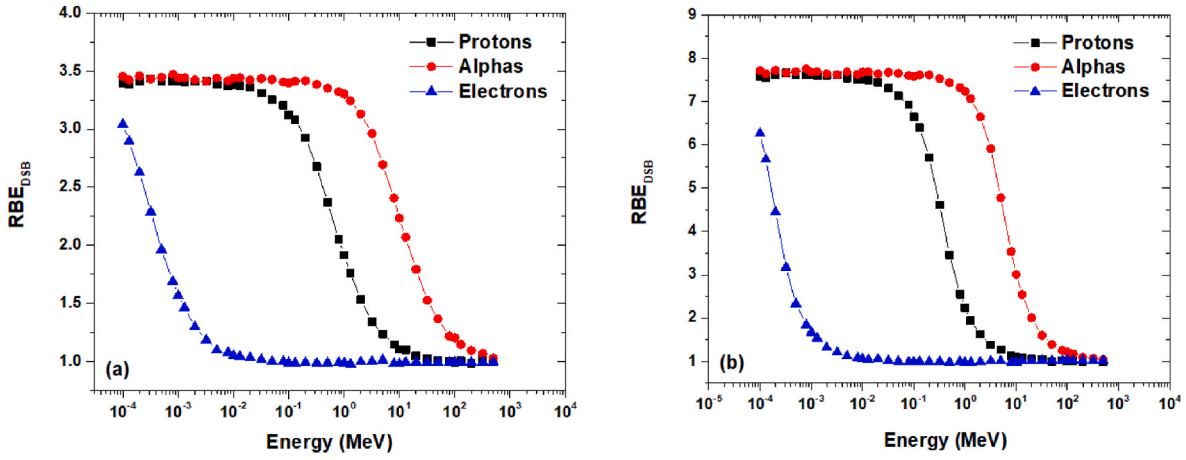

Fig. 6. MCDS calculation of relative biological effectiveness of DSB induction in cells irradiated with monoenergetic protons, alphas and electrons, under (a) aerobic and (b) severe hypoxic conditions.

range. The MCDS output files provide information about the induced number of DSB, single strand breaks (SSB) and the total yield of DSB and non-DSB clusters. MCDS results for clusters, including DSB and SSB, are normalized per unit absorbed dose (Gy) per 10^9 DNA base pairs (bp). Note that the average nuclear DNA content of a diploid human cell is about $6 \cdot 10^9$ nucleotides. The MCDS estimate of the DSB yield produced by ^{60}Co γ-rays is given in Table 4, for hypoxic and well oxygenated cells. The presented results show an increase of the SSB to DSB yield ratio from about 23 under aerobic conditions to 35.5 under the studied severe hypoxic conditions (as in some tumors).

Simulations were performed for monoenergetic charged particles with energies varying from 100 eV to 500 MeV. The findings for the studied aerobic and hypoxic conditions are presented in Fig. 6(a) and (b), respectively. The predicted RBE values for DSB production largely depend on Z_{eff}/β^2, where Z_{eff} is the effective charge of the ion and β is the speed of the ion relative to the speed of light (Stewart et al., 2011, 2015). The RBE for DSB induction approaches an asymptotic value of about 3–4 for large values of Z_{eff}/β^2 (low ion kinetic energy) and to 1.0 as $(Z_{eff}/\beta)^2$ approaches unity (large ion kinetic energies). Under hypoxic conditions, indirect (radical) damage to the DNA is reduced, which also decreases DNA damage of ^{60}Co γ-ray fields (e.g. Table 4) and higher LET ions. However, the reduction of the indirects of radiation on DNA damage are more significant for low LET radiations than for high LET ions. The net effect of the indirect effect on the induction of low and high LET radiations on DNA damage has a differential and complicated impact on the RBE for DSB induction, since it depends on the ion type, kinetic energy, pO_2 level and local environment (material composition and density).

In an attempt to estimate the dose-weighted RBE values for the neutron beams of interest, the MCNP 6.1 code was used to account for neutron transport, while appropriate correction factors obtained by the MCDS were used to account for RBE and spatial variation in dose for each particle type of interest, as outlined in (Stewart et al., 2015). The dose-weighted RBE is given by:

$$RBE = \frac{f6\ (dose \times RBE)}{f6\ (dose)} \tag{11}$$

where $f6\ (dose \times RBE)$ is the scoring tally used in MCNP for estimation of dose (tally f6) corrected by using the parameters mentioned in "RBE x Dose Tallies in MCNP 6.1" computed using the MCDS (Stewart et al., 2011) and summarized in (Stewart et al., 2015). The dose-averaged RBE for DSB induction in Gd-free cells under aerobic conditions of the three neutron beams of interest and for monoenergetic thermal neutrons are presented in Table 5. The corresponding results for 1000 ppm Gd concentration resulted in almost the same values. As shown in Table 5, the dose averaged RBE values obtained for the proton dose component from

Table 5
Dose averaged RBE_{DSB} values for secondary protons and electrons for soft tissue under aerobic conditions, along with the effective RBE values calculated by: ff. $RBE = RBE_i \times f6(dose)_i / \sum_i f6(dose)_i$, where i: protons or electrons.

Neutrons	Dose averaged RBE_{DSB}		Effective
	Protons	Electrons	RBE_{DSB}
ICON	2.99 ± 0.85	1.57 ± 0.02	1.58 ± 0.02
0.025 eV	2.99 ± 1.19	1.59 ± 0.02	1.60 ± 0.02
NEUTRA	2.65 ± 0.01	1.60 ± 0.04	2.64 ± 0.01
HK1	3.25 ± 0.01	1.60 ± 0.04	3.24 ± 0.01

0.025 eV neutrons and the ICON beams present large uncertainties, however, the effective RBE is mostly affected by electrons produced mainly outside the cell monolayer. In contrast, for HK1 and NEUTRA spectra, the protons are the primary contributors of the effective RBE. It should be noted that for alpha particles, only the NEUTRA spectrum yielded a non-zero dose-averaged RBE (not given in Table 5), but with high uncertainty. The corresponding dose averaged RBE values calculated for soft tissue loaded with 1000 ppm ^{nat}Gd yield in no significant difference compared to the RBE in the Gd-free material.

According to ref (Moertel et al., 2004). the calculated RBE_{DSB} for U-138MG human glioblastoma cells exposed to 5.7 and 7.0 MeV protons (LET 7.27 and 6.23 keV/μm, respectively) 24 h post-exposure was found to be 2.63 ± 0.07, while the RBE for 10 % survival was 1.78 ± 0.09. This, implies that the biological efficiency for tumor cell killing for other doses and *in vivo* will be high as well. This, aligns well with the present MCDS simulation results, conducted under similar conditions, which predict comparable DNA damage and RBE values in case of NEUTRA and HK1 beams, further validating the present results. In the case of lower-energy secondary protons, clusters of DNA lesions are more complex (larger number of individual nucleotides damaged per base pair) and challenging to repair, therefore, these effects may further increase the effective RBE of NCT.

6. Conclusions

A multiscale Monte Carlo model that spans cellular and sub-cellular microdosimetry in a larger-scale cell culture model is presented to facilitate the design and interpretation of NCT experiments with and without Gd as a way to boost potential treatment effectiveness. The presented model was used to design a series of experiments to evaluate the cell-killing potential of novel NCT treatments. Although Gd is a promising candidate for NCT, the loading of Gd into a cell monolayer, as in the framework of the FRINGE project (FRINGE project), it does not

yield any substantial enhancement in either the dose or the RBE-weighted dose. The present study looks at the dosimetry and biological effects of NCT across multiple scales, ranging from the sub-cellular to the larger scale details of the specific irradiation conditions for *in vitro* NCT experiments. The implemented methods are potentially useful for the design and analysis of many other *in vitro* and *in vivo* experiments.

CRediT authorship contribution statement

A. Kalamara: Writing – original draft, Visualization, Validation, Software, Methodology, Investigation, Formal analysis, Data curation, Conceptualization. **I.E. Stamatelatos:** Writing – review & editing, Validation, Supervision, Project administration, Methodology, Investigation, Conceptualization. **K.L. Stefanopoulos:** Writing – review & editing, Validation, Supervision, Methodology, Investigation, Conceptualization. **J.A. Kalef-Ezra:** Writing – review & editing, Methodology. **A.G. Georgakilas:** Writing – review & editing, Methodology. **R.D. Stewart:** Writing – review & editing, Software, Methodology. **V. Rangos:** Writing – review & editing, Methodology, Data curation. **K.D. Knudsen:** Writing – review & editing. **G. Helgesen:** Writing – review & editing. **P. Trtik:** Writing – review & editing, Methodology. **D. Mannes:** Writing – review & editing, Methodology. **J. Hovind:** Writing – review & editing, Methodology. **A. Kaestner:** Writing – review & editing, Methodology. **M. Strobl:** Writing – review & editing, Methodology. **M. Vinš:** Writing – review & editing, Methodology. **V. Klupák:** Writing – review & editing, Methodology. **M. Rabochová:** Writing – review & editing, Methodology. **J. Šoltés:** Writing – review & editing, Methodology, Investigation. **J. Milčák:** Writing – review & editing, Methodology. **M. Grigalavicius:** Writing – review & editing, Methodology. **T.A. Theodossiou:** Writing – review & editing, Project administration, Methodology, Investigation, Funding acquisition, Conceptualization.

Declaration of competing interest

The authors declare that they have no known competing financial interests or personal relationships that could have appeared to influence the work reported in this paper.

Acknowledgments

This work was done in the framework of the FRINGE project (https://www.fringe-fetopen.eu/), which has received funding from the European Union's Horizon 2020 research and innovation programme under grant agreement No 828922.

AGG acknowledges funding from project BIOSPHERE (No. 21GRD02) that has received funding from the European Partnership on Metrology, co-financed by the European Union's Horizon Europe Research and Innovation Programme and by the Participating States.

The presented results were obtained using the CICRR infrastructure, which is financially supported by the Czech Republic Ministry of Education, Youth and Sports - project LM2023041.

Data availability

Data will be made available on request.

References

Ali, M.A., et al., 1994. Properties of the ^{158}Gd compound state gamma-decay cascades. J. Phys. G Nucl. Part. Phys. 20, 1943–1953. https://doi.org/10.1088/0954-3899/20/12/010.

Allen, B.J., et al., 1989. Neutron capture therapy with gadolinium-157. Strahlenther. Onkol. 165, 156–158.

Antoni, R., et al., 2019. Microdosimetric spectra simulated with MCNP6.1 with INCL4/ABLA model for kerma and mean quality factor assessment, for neutrons between 100 keV to 19 MeV. Radiat. Meas. 128, 106189. https://doi.org/10.1016/j.radmeas.2019.106189.

Brugger, R.M., Shih, J.A., 1989. Evaluation of gadolinium-157 as a neutron capture therapy agent. Strahlenther. Onkol. 165, 153–156.

Cerullo, N., et al., 2009. Progress in the use of gadolinium for NCT. Appl. Radiat. Isot. 67, S157–S160. https://doi.org/10.1016/j.apradiso.2009.03.109.

Coghlan, W.A., et al., 1973. Auger catalog calculated transition energies listed by energy and element. Atom. Data 5, 317–469. https://doi.org/10.1016/S0092-640X(73)80005-1.

International Commission on Radiological Protection (ICRP). Composition of soft tissue. URL: https://physics.nist.gov/cgi-bin/Star/compos.pl?matno=261.

De Stasio, G., et al., 2005. Are gadolinium contrast agents suitable for gadolinium neutron capture therapy? Neurol. Res. 27 (4), 387–398. https://doi.org/10.1179/016164105X17206.

Deagostino, A., et al., 2016. Insights into the use of gadolinium and gadolinium/boron-based agents in imaging-guided neutron capture therapy applications. Future Med. Chem. 8, 899–917. https://doi.org/10.4155/fmc-2016-0022.

Dymova, M.A., et al., 2020. Boron neutron capture therapy: current status and future perspectives. Cancer Commun. 40 (9), 406–421. https://doi.org/10.1002/cac2.12089.

Enger, S.A., et al., 2013. Dosimetry for gadolinium neutron capture therapy (GdNCT). Radiat. Meas. 59, 233–240. https://doi.org/10.1016/j.radmeas.2013.05.009.

FRINGE project. URL: https://www.fringe-fetopen.eu/.

Golshani, M., et al., 2022. Gadolinium neutron capture therapy: calculation of ^{157}Gd kerma factor and a dosimetry study using MCNP Monte Carlo code. Radiat. Phys. Chem. 197, 110155. https://doi.org/10.1016/j.radphyschem.2022.110155.

Goorley, T., et al., 2004. Calculated DNA damage from gadolinium Auger electrons and relation to dose distributions in a head phantom. Int. J. Radiat. Biol. 80 (11–12), 933–940. https://doi.org/10.1080/09553000400017564.

Harms, A.A., et al., 1974. Isotopic conversion in gadolinium-exposure neutron imaging. Nucl. Instrum. Methods 118, 583–587. https://doi.org/10.1016/0029-554X(74)90669-7.

Ho, S.L., et al., 2020. In vivo neutron capture therapy of cancer using ultrasmall gadolinium oxide nanoparticles with cancer-targeting ability. RSC Adv. 10, 865–874. https://doi.org/10.1039/c9ra08961f.

Initial MCNP6 Release Overview MCNP6 Version 1.0, Los Alamos National Laboratory Report LA-U13-22934, 2013.

Ho, S.L., et al., 2022. Gadolinium neutron capture therapy (GdNCT) agents from molecular to nano: current status and perspectives. ACS Omega 7 (3), 2533–2553. https://doi.org/10.1021/acsomega.1c06603.

Kaestner, A., et al., 2011. The ICON beamline - A facility for cold neutron imaging at SINQ. Nucl. Instrum. Methods Phys. Res. A 659 (1), 387–393. https://doi.org/10.1016/j.nima.2011.08.022.

Lehmann, E., et al., 2001. Properties of the radiography facility NEUTRA at SINQ and its potential for use as European reference facility. Nondestr. Test Eval. 16 (2–6), 191–202. https://doi.org/10.1080/10589750108953075.

Marek, M., et al., 2014. Extended set of activation monitors for NCT beam characterization and spectral conditions of the beam after reactor fuel conversion. Appl. Radiat. Isot. 88, 157–161. https://doi.org/10.1016/j.apradiso.2013.11.040.

Miller, G.A., et al., 1993. Gadolinium neutron capture therapy. Nucl. Technol. 103, 320–331. https://doi.org/10.13182/NT93-A34855.

Moertel, H., et al., 2004. Effects of low energy protons on clonogenic survival, DSB repair and cell cycle in human glioblastoma cells and B14 fibroblasts. Radiother. Oncol. 73, S115–S118. https://doi.org/10.1016/S0167-8140(04)80030-6.

Q-value calculator (QCalc) by National Nuclear Data Center. URL: https://www.nndc.bnl.gov/qcalc/.

Sakurai, Y., et al., 2002. Experimental verification of the nuclear data of gadolinium for neutron capture therapy. J. Nucl. Sci. Technol. (Suppl. 2), 1294–1297. https://doi.org/10.1080/00223131.2002.10875341.

Santa Cruz, G.A., 2016. Microdosimetry: principles and applications. Rep. Practical Oncol. Radiother. 21 (2), 135–139. https://doi.org/10.1016/j.rpor.2014.10.006.

Schultz, D., et al., 2010. The K-shell Auger electron spectrum of gadolinium obtained using neutron capture in a solid state device. J. Phys. D Appl. Phys. 43, 075502. https://doi.org/10.1088/0022-3727/43/7/075502.

Semenenko, V.A., Stewart, R.D., 2004. A fast Monte Carlo algorithm to simulate the spectrum of DNA damage formed by ionizing radiation. Radiat. Res. 161 (4), 451–457. https://doi.org/10.1667/rr3140.

Semenenko, V.A., Stewart, R.D., 2006. Fast Monte Carlo simulation of DNA damage formed by electrons and light ions. Phys. Med. Biol. 51 (7), 1693–1706. https://doi.org/10.1088/0031-9155/51/7/004.

Shih, J.A., Brugger, R.M., 1992. Gadolinium as a neutron capture therapy agent. Med. Phys. 19 (3), 733–744. https://doi.org/10.1118/1.596817.

Stewart, R.D., et al., 2011. Effects of radiation quality and oxygen on clustered DNA lesions and cell death. Radiat. Res. 176, 587–602. https://doi.org/10.1667/rr2663.1.

Stewart, R.D., et al., 2015. Rapid MCNP simulation on DNA double strand break (DSB) relative biological effectiveness (RBE) for photons, neutrons and light ions. Phys. Med. Biol. 60, 8249–9274. https://doi.org/10.1088/0031-9155/60/21/8249.

Tung, C.J., 2015. Microdosimetric relative biological effectiveness of therapeutic proton beams. Biomed. J. 38 (5), 399–407. https://doi.org/10.4103/2319-4170.167072.

Van Delinder, K.W., et al., 2020. Neutron activation of gadolinium for ion therapy: a Monte Carlo study of charged particle beams. Sci. Rep. 10, 13417. https://doi.org/10.1038/s41598-020-70429-9.

6x3 well-plate, 6x3 well-plate. https://ibidi.com/chambered-coverslips/236–slide-18-well.html.

Yasui, L.S., et al., 2008. Gadolinium neutron capture in glioblastoma multiforme cells. Int. J. Radiat. Biol. 84 (12), 1130–1139. https://doi.org/10.1080/09553000802538092.